Research Article | Vol. 31, No. 5 / 27 Feb 2023 / Optics Express 7632
Optics EXPRESS

Radial-mode sensitive probe beam in the rotational Doppler effect

ZHENYU GUO,[1,†] ZEHONG CHANG,[1,†] YING ZHANG,[1] GUANGDONG MA,[1] XINDONG ZHU,[1] JUNLIANG JIA,[1,*] AND PEI ZHANG[1,2,3]

[1] *Ministry of Education Key Laboratory for Nonequilibrium Synthesis and Modulation of Condensed Matter, Shaanxi Province Key Laboratory of Quantum Information and Quantum Optoelectronic Devices, School of Physics, Xi'an Jiaotong University, Xi'an 710049, China*
[2] *State Key Laboratory of Applied Optics, Changchun Institute of Optics, Fine Mechanics and Physics, Chinese Academy of Sciences, Changchun 130033, China*
[3] *zhangpei@mail.ustc.edu.cn*
[†] These authors contributed equally to this work
[*] *junliang22@xjtu.edu.cn*

Abstract: The rotational Doppler effect (RDE) attracts much attention in various research areas, from acoustics to optics. The observation of RDE mostly depends on the orbital angular momentum of the probe beam, while the impression of radial mode is ambiguous. To clarify the role of radial modes in RDE detection, we reveal the mechanism of interaction between probe beams and rotating objects based on complete Laguerre-Gaussian (LG) modes. It is theoretically and experimentally proved that radial LG modes play a crucial role in RDE observation because of topological spectroscopic orthogonality between probe beams and objects. We enhance the probe beam by employing multiple radial LG modes, which makes the RDE detection sensitive to objects containing complicated radial structures. In addition, a specific method to estimate the efficiency of various probe beams is proposed. This work has the potential to modify RDE detection method and take the related applications to a new platform.

1. Introduction

The Doppler effect is one of the most remarkable frequency shift effect introduced by relative motion in line. Therein a rotational Doppler effect (RDE) is the phenomena induced by relative rotational motion between the source and the observer [1]. RDE relies on an oblique Poynting vector that requires the incident beam to carry either spin angular momentum [2–4] or orbital angular momentum (OAM) [5–8]. So far, RDE has been observed from beams transmitted through half waveplate [9], nonlinear crystal disk [10], Dove prism [11], spiral phase plates [12], and engraved scattering rough surface [13], etc. The amount of spin angular momentum is restricted to $\pm\hbar$ per photon, while OAM described with a helical wavefront $e^{i\ell\phi}$ is proved to carry an amount of angular momentum $\ell\hbar$ per photon, where ℓ is the topological charge and ϕ is the azimuthal coordinate. Spin-induced RDE is relatively weak for its small topological charges ± 1 which limits the prospects in applications. In comparison, OAM-induced RDE can be very intense for its theoretically unlimited topological charges [14]. Therefore, OAM-induced RDE inspires more applications such as analyzation of OAM spectrum [15], characterization of fluid vortex types [16], detection and demultiplexing of cylindrical vector beams [17], nonreciprocal control of acoustic OAM [18], and far-field detection of rotating objects [19–27].

It is worth mentioning that far-field detection of rotating objects is one of the rapidly developing applications of RDE techniques. In 2013, Lavery *et al.* present a seminal work to measure remote rotation speed by analyzing the OAM of the light beam scattered from a rotating object [13], where the rotation speed can be observed by a frequency shift proportional to the topological

#482431 https://doi.org/10.1364/OE.482431
Journal © 2023 Received 1 Dec 2022; revised 16 Jan 2023; accepted 30 Jan 2023; published 15 Feb 2023

Optics EXPRESS

charge of OAM of the light beam. This frequency shift is independent of the optical frequency, hence a white-light source can also contribute to a single-valued frequency shift [23]. In physics, it is clarified that RDE sources from a locally retarded position which means RDE can be explained by a local linear Doppler effect [6]. Then this proposition is improved to that RDE and linear Doppler effect can derive from each other, which is demonstrated by an exquisite experimental design where the two Doppler effects share the same origin [7].

In experiment, the long-range transmission of RDE signals and structural analysis of the rotating objects are two main challenges. On one side, signal attenuation induced by turbulence in atmosphere and the low efficiency in photon collection often obstruct the implementation of a real RDE detection system. Zhang *et al.* overcome these obstructs and establish a 120 m RDE link in outdoor environment to detect the rotational speed of remote patterns [28]. Researchers even expect that RDE signal reaches a further distance such as outer space [29]. On the other side, structural analysis refers to a complete spectral decomposition of the rotating object [30]. The above experiments only concern the OAM components of the probe beam and object, which can be defined as azimuthal modes [31–33]. However, a complete description of rotating objects must contain radial modes components [34–37]. Up to now, the generation and detection of radial modes are adequately discussed in classical and quantum realms [38–42]. It is found that radial modes are meaningful in many applications such as optical manipulation, high-dimensional entanglement, and quantum fundamental verification [43–45]. The absence of radial mode leads to insufficient exploitation of the information about an object, which restricts the development of RDE detection [46]. Here we clarify the radial interaction between a probe beam and a rotating object. With the help of this interaction, the probe beam can be improved to greatly enhance the intensity of the final signal in RDE detection and extract more structural information about the rotating object.

In this paper, we propose a radial-modes sensitive probe beam and establish a complete physical description of the interaction between the probe beam and rotating object in RDE detection system. We also propose a formula to estimate the mode utilization rate synergizing the LG components of both probe beam and rotating object. The propositions are demonstrated by a two-step experiment. Firstly, two presupposed simple rotating objects are employed to examine the efficiency of both traditional and enhanced probe beams. Then a complex jellyfish pattern is successfully observed in the RDE detection system. The experiment distinctly shows that a radial-modes sensitive probe beam is stronger than a traditional probe beam in the detection of objects with complex radial structures.

2. Probe beam and probe efficiency

Laguerre-Gaussian (LG) mode is one of the most widely used probe beams in RDE detecting frame, which can be defined in the cylindrical coordinates as follows:

$$\begin{aligned} LG_p^{\ell}(r,\varphi,z) =& E_0 \frac{w_0}{w(z)} \left(\frac{\sqrt{2}r}{w(z)}\right)^{|\ell|} L_p^{|\ell|}\left(\frac{2r^2}{w^2(z)}\right) \\ & \times e^{\frac{-r^2}{w^2(z)}} \times e^{-\frac{ikr^2}{2R(z)}+i(2p+|\ell|+1)\Phi(z)-i\ell\varphi}, \end{aligned} \tag{1}$$

where E_0 is a constant, $w(z)$ is the beam width, w_0 is the waist width, $L_p^{|\ell|}$ represents the associated Laguerre polynomials with p and ℓ the radial and azimuthal indices, k is the wave number, $R(z)$ is the radius of curvature, and $\Phi(z)$ marks the Gouy phase respectively. LG mode is a solution of the paraxial Helmholtz equation, so it can propagate stably in free space [47]. Vortex beam with helical phase structure $e^{i\ell\varphi}$ is a significant subset of LG mode, which is employed in many seminal works [13]. Early works think little of radial dimension which is of vital importance in the interaction with a real object. For the sake of detecting the RDE of a radial inhomogeneous

Optics EXPRESS

object, LG mode with the definition of radial index p is to be considered. In addition, LG mode possesses the orthogonal completeness of both radial and angular dimensions, so it is the best choice to study radial RDE in both quantum and classical realms.

The rotating object is another key element in RDE detecting frame, which can be expressed with a superposition of LG modes [30]. It means that a rotating object can be safely described as the LG modes-based modulation

$$\mathrm{O}(r,\varphi,t)=\sum_{\ell,p}A_{\ell,p}\mathrm{LG}_p^{\ell}(r,\varphi)e^{-i\ell\Omega t}, \tag{2}$$

where complex number $A_{\ell,p}$ is composed with the weighting coefficient $\left|A_{\ell,p}\right|$ and initial phase ϕ, Ω represents the rotating speed of the object. Four representative objects are displayed in Fig. 1(a~d). The first object O_1 (Fig. 1(a)) is constructed with LG modes $\{LG_1^{-6}, LG_0^{-3}, LG_2^{-3}, LG_0^{0}, LG_0^{3}, LG_1^{3}, LG_1^{6}\}$ with weights {0.1, 0.5, 0.2, 1, 0.5, 0.2, 0.1} normalized by the amplitude of LG_0^0. The second object O_2 (Fig. 1(b)) is constructed with LG modes $\{LG_0^{-5}, LG_2^{-5}, LG_0^{0}, LG_0^{5}, LG_1^{5}\}$ with weights {0.5, 0.3, 1, 0.5, 0.3} also normalized by the amplitude of LG_0^0. The third object O_3 (Fig. 1(c)) is composed with LG modes $\{LG_1^{-3}, LG_0^{-5}, LG_0^{0}, LG_0^{-3}, LG_0^{3}, LG_2^{1}\}$ with weighting coefficients {1, 1, 0.625, 0.25, 0.25, 1} normalized by the amplitude of LG_1^{-3}. The fourth object O_4 (Fig. 1(d)) is composed with LG modes $\{LG_1^{-3}, LG_0^{-5}, LG_0^{0}, LG_0^{-3}, LG_2^{-1}, LG_0^{-6}, LG_1^{-4}, LG_2^{-2}\}$ with weighting coefficients {0.125, 0.125, 1, 0.125, 0.125, 1, 1, 1} normalized by the amplitude of LG_0^0. The first two types exhibit geometrical distributions almost unrelated to radial coordinate on account of the small weights of LG modes of $p\neq 0$ relative to $p=0$. In contrast, the last two objects contain $p\neq 0$ LG modes with large weights, so that potentially convey more luxuriant radial interaction.

ℓ and p indices of LG modes simultaneously construct an N index to define an enhanced probe beam. It is worth noting that an N-order probe beam is expressed with

$$\mathrm{P}(r,\varphi)=\sum_{\ell,p}B_{\ell,p}\mathrm{LG}_p^{\ell}(r,\varphi), \tag{3}$$

based on Eq. (1), where ℓ and p satisfy $N=2p+|\ell|$; $B_{\ell,p}$ is normalized with $\sum_{\ell,p}B_{\ell,p}^{*}B_{\ell,p}=1$. Take a traditional probe beam $\mathrm{P}_1=\frac{1}{\sqrt{2}}\left(LG_0^{\ell}+LG_0^{-\ell}\right)$ as an example, which is also called the petals-like beam. It involves two LG modes of azimuthal index $\pm\ell$ and is sensitive to angular motion so it is frequently found in previous research [13]. Because of the orthogonality of LG modes, only a part of LG components in the rotating object take effects in producing beating signals in the interaction with the probe beam. The main output signal of the rotating object may be understood via the equation

$$\begin{aligned}I(t)&=\left|\iint \mathrm{P}_1\mathrm{O}(r,\varphi,t)rdrd\varphi\right|^2\\&=\frac{1}{2}\left|A_{-\ell,0}e^{i\ell\Omega t}\iint\left(LG_0^{\ell}\right)^{*}LG_0^{\ell}rdrd\varphi+A_{\ell,0}e^{-i\ell\Omega t}\iint\left(LG_0^{-\ell}\right)^{*}LG_0^{-\ell}rdrd\varphi\right|^2\\&=\frac{1}{2}\left(\left|A_{\ell,0}\right|^2+\left|A_{-\ell,0}\right|^2\right)+\left|A_{\ell,0}\right|\left|A_{-\ell,0}\right|\cos\left(2\ell\Omega t+\phi_0+\phi_1\right)\end{aligned} \tag{4}$$

where $A_{-\ell,0}=|A_{-\ell,0}|e^{i\phi_0}$, $A_{\ell,0}=|A_{\ell,0}|e^{-i\phi_1}$, and $\iint LG_0^{\ell *}LG_0^{\ell}rdrd\phi=1$ ensure the result is correct. It is worth noting that on the plane where $z=0$, $(LG_p^{\ell})^{*}=LG_p^{-\ell}$. Obviously, the computed trigonometric function reveals a beating signal of optical intensity, which is an important observable value in RDE detection. Comparing with Eq. (2), we see that only two components LG_0^{ℓ} and $LG_0^{-\ell}$ contribute to the last beating signal. The leading components in O_1

Optics EXPRESS

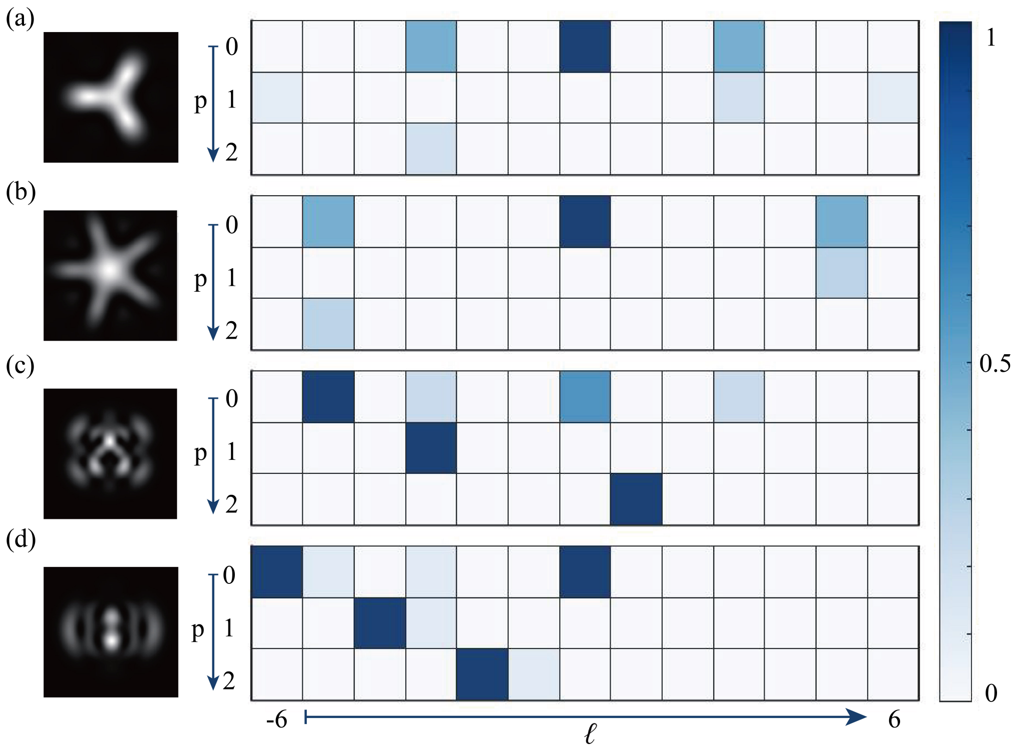

Fig. 1. LG modes decompositions of the rotating objects, synergizing both ℓ and p indices. **(a)** and **(b)** represent objects with large $|A_{\ell,0}|$ and $|A_{-\ell,0}|$ components, which is sensitive to a petals-like probe beam P_1. **(c)** and **(d)** represent objects with complicated radial distributions, which is almost invisible to former probe beam.

and O_2 are $\{LG_0^{-3}, LG_0^3\}$ and $\{LG_0^{-5}, LG_0^5\}$ respectively. Consequently, when $\ell = 3$ or $\ell = 5$, we can safely claim that probe beams P_1 are sensitive to the objects O_1 or O_2 respectively by Eq. (4).

However, these symmetric leading components are not always present in real objects. For example, O_3 (Fig. 1(c)) and O_4 (Fig. 1(d)) contain multiple leading components $\{LG_0^{-5}, LG_1^{-3}, LG_2^1\}$ and $\{LG_0^{-6}, LG_1^{-4}, LG_2^{-2}\}$ respectively. They are not sensitive to probe beam P_1 on account of the orthogonality between LG modes. In this situation, how to find an enhanced probe beam to sense these objects is a meaningful problem.

We recognize that the effectiveness of a probe beam defined with Eq. (3) is determined by its effective LG components concerning the rotating objects. A probe can be enhanced by covering more LG components, which is specifically shown in Fig. (2). The probe beam is a significant module in the schematic diagram of RDE detection, which is then incident to a rotating object and measured by an intensity collector. A traditional probe beam like P_1 can be extended to multiple LG modes with $p \neq 0$. As shown in Fig. (2), a probe beam composed of the left two profiles can be enhanced into a probe beam composed of the right four profiles which is also the largest effective probe beam of Eq. (3). In this extension, radial components of the rotating object are sufficiently considered in the last intensity measurement.

Optics EXPRESS

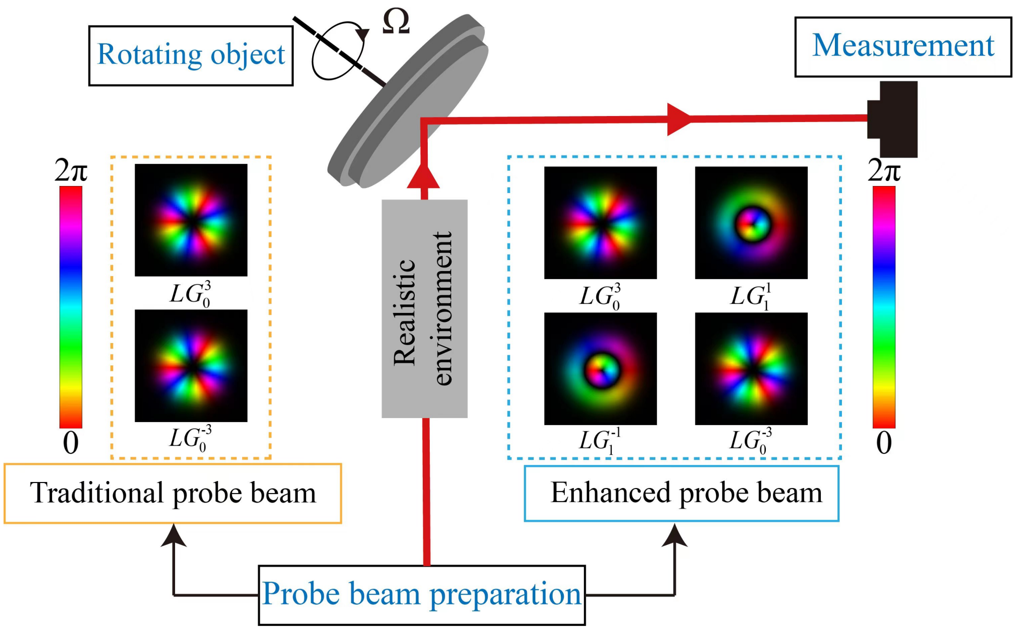

Fig. 2. The schematic diagram employed to remotely measure the rotational speed of an object based on RDE. The left two profiles are the LG modes included in the traditional probe beam while the right four profiles are to be included in an extended probe beam. All LG modes are kept in the same order $N = 3$.

The intensity measurement is mainly dependent on the beating signal, which is collected in the basic Gaussian mode after the conversion shown in the schematic diagram, specifically

$$
\begin{aligned}
I(t) &= \left| \iint \mathrm{P}(r,\varphi)\mathrm{O}(r,\varphi,t) r dr d\varphi \right|^2 \\
&= \left| \begin{array}{l} B_{l,p}A_{-l,p}e^{il\Omega t} \iint LG_p^{-\ell *} LG_p^{-\ell} r dr d\varphi + \\ B_{l+2,p-1}A_{-l-2,p-1}e^{i(l+2)\Omega t} \iint LG_{p-1}^{-\ell-2*} LG_{p-1}^{-\ell-2} r dr d\varphi \\ + \ldots\ldots + B_{-l,p}A_{l,p}e^{-il\Omega t} \iint LG_p^{\ell *} LG_p^{\ell} r dr d\varphi \end{array} \right|^2 \\
&= \left| \sum_{l,p} B_{l,p}A_{-l,p}e^{il\Omega t} \right|^2 .
\end{aligned}
\tag{5}
$$

The corresponding RDE frequency shifts related to the periods of trigonometic components can be obtained by a Fourier transform.

It is found that the enhanced probe beam has two main advantages over the traditional one. The first point is that it is sensitive to the radial modes of the rotating object, which reaches a new plateau in the utilization of LG modes. The second point is that it completely reflects the interaction between the probe beam and the rotating object based on LG modes, so it is possible to define a valid standard constant to evaluate the probe beam in RDE detection. In ideal conditions, the probe beam in an arbitrary RDE detection system possesses a certain constant

$$R = \frac{\sum_{\ell,p} \left| A_{-\ell,p} B_{\ell,p} \right|}{\sqrt{\left(\sum_{\ell,p} A^*_{\ell,p} A_{\ell,p} \right) \left(\sum_{\ell,p} B^*_{\ell,p} B_{\ell,p} \right)}}. \tag{6}$$

It can be considered as a reference in the selection of probe beam in a certain RDE detection task.

For a given mode order N, the number of LG modes that can be included in probe beams is $2 * \mathrm{int}\left(\frac{N+1}{2}\right)$, where $N \geq 1$. As shown in Fig. 2, when the mode order $N = 3$, four LG modes $\{LG_0^3, LG_1^1, LG_1^{-1}, LG_0^{-3}\}$ are available. It is worth noting that LG modes with index $\ell = 0$ are not in this collection for lacking a helical wavefront.

The normalization in Eq. (3) guarantees the amplitude of light incident to the rotating object is standard, which provides a fair comparison for different probe beams. In this case, the power ratio is mainly determined by the modulation effect of object according to Eq. (6). Considering probe beam P_1 (with $\ell = 3$) and object O_1, we see that Eq. (6) gives a valid standard ratio 0.559, while the ratio is 0.189 for O_3. It is obvious that the effectiveness of probe beam P_1 for object O_3 is worse than that for object O_1. In an extreme situation, the standard ratio of probe beam P_1 is 0 for object O_4, meaning that P_1 has no effect on this specific object. All these facts tell us that an enhanced probe beam can present some interesting information.

It is true that the Fourier spectrum of beating signals of the enhanced probe beam can be more complex than that of the traditional probe beam, but due to the exploitation of more information about the object, the expected main frequency peak intends to be enhanced. Let alone diverse characteristics of the rotating object are possible to be exhibited by the Fourier spectrum.

3. Experimental results and discussion

The probe beam preparation, the rotating object, and the intensity measurement as shown in Fig. 2 are implemented in a proof-of-principle experiment. Figure 3 displays the setup of this experiment. A He-Ne laser pumps a light beam with wavelength $\lambda = 633$ nm. The beam passes through a half-wave plate (HWP) and a polarized beam splitter (PBS), which is employed to control the intensity incident and initial the beam in horizontal polarization. Two lenses (L1 and L2) construct a $\times 6$ expander and collimate the beam with the first spatial light modulator (SLM1, UPOlabs HDSLM80R). A computer-generated hologram [48] loaded on SLM1 is used to generate the probe beams with exact amplitudes and phases of LG components. Fig. 3(d) shows an example of hologram producing probe beam $P(r, \varphi) = \frac{1}{\sqrt{2}}\left(LG_0^5 + LG_1^3\right)$. The probe beams are selected in the first diffraction order by lenses L3, L4, and a pinhole (P). Then the probe beams illuminate the object which is loaded on SLM2 (Meadowlark P1920-635-HDMI). Fig. 3(e) shows an example of hologram mimicking object O_3. Note that the rotation of the object is mimicked by the rotation of the content of hologram, where the rotation speed is set in $\Omega = 2\pi$ rad/s by periodically switching holograms of stepping angles. In reality, SLM2 modulates vertical polarization while SLM1 modulates horizontal polarization, so an HWP is included to change horizontal polarization to vertical one. After the scattering of the rotating object, L5 and L6 couple the basic Gaussian component of the output beam to the single mode fiber (SMF), where the coupling efficiency of incident basic Gaussian mode is about fifty percent. Finally, a power meter connected to the SMF is used to record the time-dependent intensities, which are computed by fast Fourier transform (FFT) to obtain the frequency spectrum of the beating signal.

The experiment is implemented in two steps. Firstly, we design a series of probe beams to illuminate rotating objects O_3 and O_4 as shown in Fig. 1(c) and (d) to verify the beating frequency

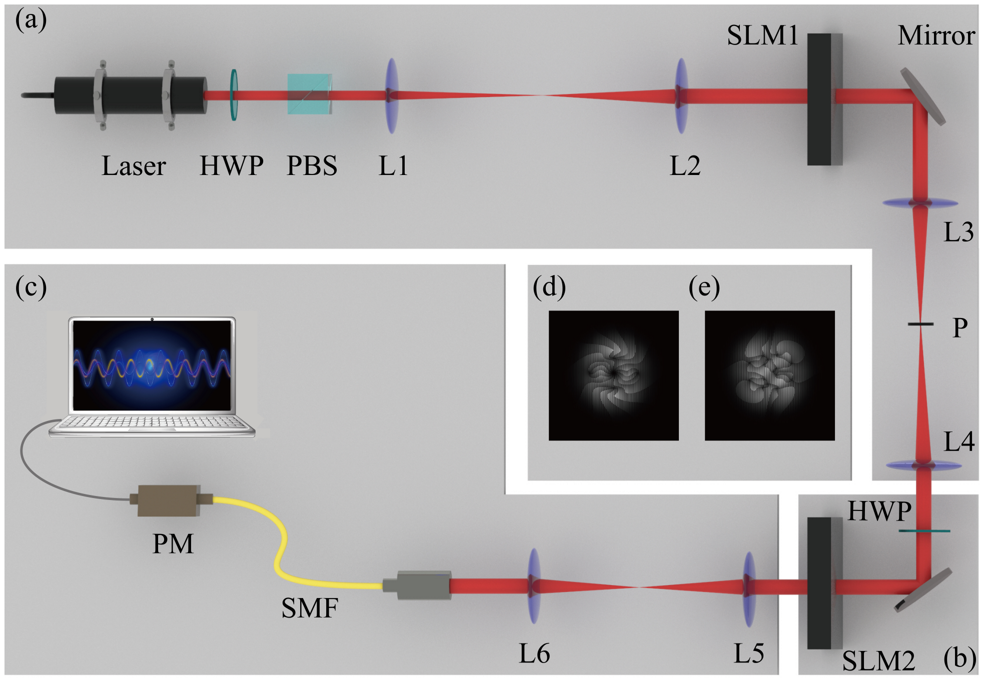

Fig. 3. Setup of the experiment. HWP, half-wave plate; PBS, polarized beam splitter; SLM, phase-only spatial light modulator; P, pinhole; L1-L6, thin lenses. SMF, single mode fiber; PM, power meter. (a) Generation of probe beams. (b) Rotating objects. (c) Signal collection. (d) and (e) display holograms loaded on SLM1 and SLM2 respectively.

of them. In the test of object O_3, the collection of probe beams contains traditional probe beams $P_1(\ell)$ (with $\ell = 1, 2, 3, 4, 5$) and an enhanced probe beam $P(r, \varphi) = \frac{1}{\sqrt{2}}\left(LG_0^5 + LG_1^3\right)$. The measured beating signals are shown in Fig. 4(a), representing collected intensities depending on the rotation angles of the object O_3. They are transformed to frequency domain as shown in Fig. 4(c) by FFT. There is no abrupt peak for probe beams $P_1(\ell)$, which is in good agreement with the theory. This is because the most related coefficients $|A_{\ell,0}|$ and $|A_{-\ell,0}|$ only make up little weight in the mimicked rotating object of SLM2. According to Eq. (4), the amplitude of the cosine function is approximately zero in theory. It means that the traditional probe beams can not adequately exploit the information of rotating objects to obtain intensive beating signals. In contrast, the enhanced probe beam provides coefficients $B_{5,0} = B_{3,1} = \frac{1}{\sqrt{2}}$, which adequately interacts with LG components LG_0^{-5} and LG_1^{-3} whose amplitudes $|A_{-5,0}| = |A_{-3,1}| = 1$. According to Eq. (5), their beating intensity $I(\mathrm{t}) \propto 1 + \cos(4\pi t)$, where the beat frequency induced by RDE should be 2 Hz, which is consistent with the data shown in Fig. 4(c). When the probe beam is $P_1(\ell)$, faint undesirable peaks can still be observed, which we attribute to the energy transfer of the dominant mode to the adjacent mode [26,28]. There are two main experimental reasons for this. First, the spiral spectrum of the object to be detected generated by SLM2 is extended compared to the expected spectrum because the beam collimation is not perfect. The second is the imperfection of OAM filtering due to the slight misalignments between the coupling fiber and the whole system.

We carry out a similar strategy for another rotating object O_4 (Fig. 1(d)). The beating signals and their Fourier transforms are shown in Fig. 4(b) and (d) respectively. In this group, a collection of probe beams is employed to illuminate the rotating object, which

Optics EXPRESS

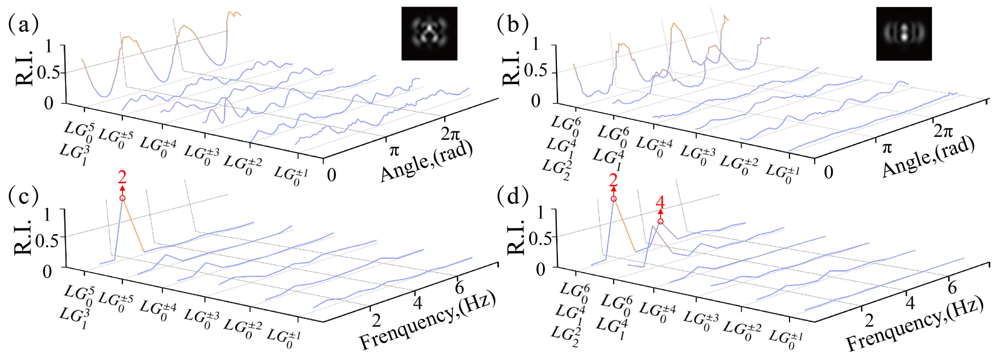

Fig. 4. Measurement of LG modes fusion. **(a)** and **(b)** represent the measured intensity depending on the rotation angle. **(c)** and **(d)** represent the corresponding RDE frequency shifts. R.I. represents the normalized relative intensity.

contains traditional probe beams $P_1(\ell)$ (with $\ell = 1, 2, 3, 4$) and two enhanced probe beams $P(r, \varphi) = \frac{1}{\sqrt{2}}\left(LG_0^6 + LG_1^4\right)$, $P'(r, \varphi) = \frac{1}{\sqrt{3}}\left(LG_0^6 + LG_1^4 + LG_2^2\right)$. Therein, the last two probe beams produce intensive beating signals. According to Eq. (5), when taking the probe beam $P(r, \varphi)$, we have $|A_{-4,1}| = |A_{-6,0}| = 1$ and $B_{4,1} = B_{6,0} = \frac{1}{\sqrt{2}}$ to compute $I(\mathrm{t}) \propto 1 + \cos(4\pi t)$; when taking the probe beam $P'(r, \varphi)$, we have $|A_{-2,2}| = |A_{-4,1}| = |A_{-6,0}| = 1$ and $B_{2,2} = B_{4,1} = B_{6,0} = \frac{1}{\sqrt{3}}$, then obtain $I(\mathrm{t}) \propto 1 + \frac{2}{3}\cos(8\pi t) + \frac{4}{3}\cos(4\pi t)$. Obviously, the probe beam $P(r, \varphi)$ produces one main beating signal with frequency 2 Hz while $P'(r, \varphi)$ produces two main beating signals with frequencies 2 Hz and 4 Hz. According to Eq. (6), it is easy to know the highest peak of $P'(r, \varphi)$ is greater than that of $P(r, \varphi)$. In reality, as shown in Fig. 4(d), only $P(r, \varphi)$ and $P'(r, \varphi)$ possess conspicuous peaks, where the peak values of $P'(r, \varphi)$ is 1 and 0.406, the peak values of $P(r, \varphi)$ are 0.616 and 0.150 respectively in 2 Hz and 4 Hz. The experimental results are coincident with the theoretical analysis. When the probe beam is $P(r, \varphi)$, the appearance of 4Hz is not expected, which we attribute to the adverse effect of the jitter in the time of data collection. During this time, any slight misalignment caused by small vibrations will cause the collected signals to deviate from expectations. Deviating signals will cause higher harmonics to occur when performing fast Fourier transforms. When the probe beam is $P'(r, \varphi)$, the theoretical peak value of 4 Hz is 0.5. The deviation between the experimental results and expectations is attributed to the different coupling efficiency of single-mode fiber under different modes [49]. One more word, the two peaks produced by $P'(r, \varphi)$ show that an enhanced probe beam utilizing more LG components are potential to observe more structural features of the rotating object.

By sensing the rotation of the above two objects, we demonstrated the critical role of radial mode in RDE detection. It is beneficial to practical applications because researchers can not only measure the speed of an object according to the main frequency peak but also read other features of the object according to the construction of multiple frequency peaks.

In the second step, we choose a real picture of jellyfish, as shown in Fig. 5(a), to present a visible phenomenon of the enhanced probe beam in practical RDE detection. The picture of jellyfish acts as a computer-generated hologram loaded on the screen of SLM2 to mimic a rotating jellyfish. Traditional probe beams $P_1(\ell)$ (with $\ell = 1, 2, 3$) are also employed in this group. Predictably, there is almost no beating signal to be detected, as shown in Fig. 5(c) and (d). Jellyfish possesses a complex and asymmetric structure, which can be decomposed into LG modes as shown in Fig. 5(b). It is found that all the LG components referring to $P_1(\ell)$ are set in low weights. Meanwhile, LG_2^1, LG_1^3, and LG_0^5 dominate the weights of LG components of the object. So we build three representative prob beams in regard to the three LG

Optics EXPRESS

modes, where $P_2 = \frac{1}{\sqrt{2}}\left(LG_1^3 + LG_0^5\right)$, $P_3 = \frac{1}{\sqrt{2}}\left(LG_2^1 + LG_1^3\right)$ and $P_4 = \frac{1}{\sqrt{3}}\left(LG_2^1 + LG_1^3 + LG_0^5\right)$ specifically. According to Eq. (6), they are all able to contribute frequency peaks in the spectrum of Fig. 5(d), where the intensity of P_4 is the greatest. In Fig. 5(d), the intensities of the Fourier spectrum are normalized by the greatest value. In the experiment, the peaks of frequency 2 Hz are 0.484, 0.540 and 1.000 for probe beams P_2, P_3 and P_4 respectively, which is in good agreement with predictions. All these phenomena confirm a radial-modes sensitive probe beam is examined by specific LG modes composition of the object referring to Eq. (6). Sincerely, the LG components with $\ell = 0$ of jellyfish are not developed enough in the analysis. But we still prove the feasibility and applicability to enhance a probe beam with radial modes. By choosing a radial-modes sensitive probe beam, we can easily acquire an intensive beating signal from a complex object in RDE detection, which is almost impossible for a traditional probe beam.

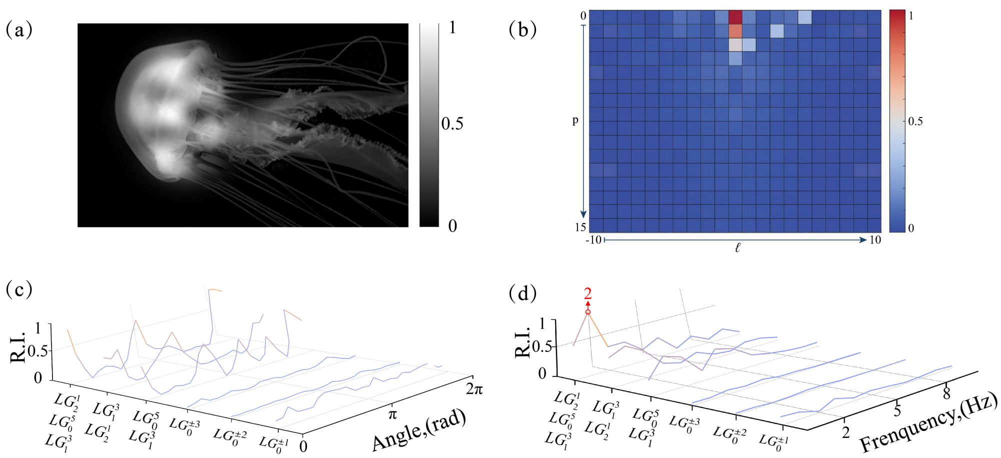

Fig. 5. **(a)** Amplitude modulation of jellyfish. **(b)** LG modes spectrum of jellyfish. **(c)** represents the measured intensity depending on the rotation angle. **(d)** represents the corresponding RDE frequency shifts. R.I. represents the normalized relative intensity.

4. Conclusion

In summary, we strictly research the effects of radial modes in the RDE detection system by theory and experiment. In this system, both probe beams and objects are decomposed into LG modes with a radial topological number p for establishing a complete description of the beating signals in detection. It is revealed that the rotating object is not always sensitive to the probe beam because of the orthogonality of LG modes. The presence of radial modes provides an effective method to construct a radial-modes sensitive probe beam. This enhanced probe beam exploits more LG components of a real object, hence its performance is better than the traditional $LG_0^{\pm\ell}$-style when the object contains a complex radial structure. On the other side, we present a formula to evaluate the efficiency of probe beams, which helps us to select an appropriate probe beam in a practical RDE detection task. This work fully develops the radial modes, so has the potential to reach a new plateau in the RDE detection method and related applications [50].

Funding. National Natural Science Foundation of China (11804271, 12174301, 91736104).

Acknowledgment. The authors thank Dr. Rui Qu and Dr. Zidan Zhao from Xian Jiaotong University for helpful technical discussions.

Disclosures. The authors declare no conflicts of interest.

Optics EXPRESS

Data Availability. Data underlying the results presented in this paper are not publicly available at this time but may be obtained from the authors upon reasonable request.

References

1. J. Courtial, D. A. Robertson, K. Dholakia, L. Allen, and M. J. Padgett, "Rotational frequency shift of a light beam," Phys. Rev. Lett. **81**(22), 4828–4830 (1998).
2. J. Deng, K. F. Li, W. Liu, and G. Li, "Cascaded rotational Doppler effect," Opt. Lett. **44**(9), 2346–2349 (2019).
3. B. A. Garetz and S. Arnold, "Variable frequency shifting of circularly polarized laser radiation via a rotating half-wave retardation plate," Opt. Commun. **31**(1), 1–3 (1979).
4. R. Simon, H. J. Kimble, and E. C. G. Sudarshan, "Evolving geometric phase and its dynamical manifestation as a frequency shift: an optical experiment," Phys. Rev. Lett. **61**(1), 19–22 (1988).
5. M. V. Vasnetsov, J. P. Torres, D. V. Petrov, and L. Torner, "Observation of the orbital angular momentum spectrum of a light beam," Opt. Lett. **28**(23), 2285–2287 (2003).
6. F. C. Speirits, M. P. J. Lavery, M. J. Padgett, and S. M. Barnett, "Optical angular momentum in a rotating frame," Opt. Lett. **39**(10), 2944–2946 (2014).
7. L. Fang, M. J. Padgett, and J. Wang, "Sharing a common origin between the rotational and linear Doppler effects," Laser Photonics Rev. **11**(6), 1700183 (2017).
8. Z. Jin, D. Janoschka, J. Deng, L. Ge, P. Dreher, B. Frank, G. Hu, J. Ni, Y. Yang, J. Li, C. Yu, D. Lei, G. Li, S. Xiao, S. Mei, H. Giessen, F. M. zu Heringdorf, and C.-W. Qiu, "Phyllotaxis-inspired nanosieves with multiplexed orbital angular momentum," eLight **1**(1), 5 (2021).
9. G. E. Sommargren, "Up/down frequency shifter for optical heterodyne interferometry," J. Opt. Soc. Am. **65**(8), 960–961 (1975).
10. G. Li, T. Zentgraf, and S. Zhang, "Rotational Doppler effect in nonlinear optics," Nat. Phys. **12**(8), 736–740 (2016).
11. J. Courtial, K. Dholakia, D. A. Robertson, L. Allen, and M. J. Padgett, "Measurement of the rotational frequency shift imparted to a rotating light beam possessing orbital angular momentum," Phys. Rev. Lett. **80**(15), 3217–3219 (1998).
12. H. Zhou, D. Fu, J. Dong, P. Zhang, and X. Zhang, "Theoretical analysis and experimental verification on optical rotational doppler effect," Opt. Express **24**(9), 10050–10056 (2016).
13. M. P. J. Lavery, F. C. Speirits, S. M. Barnett, and M. J. Padgett, "Detection of a spinning object using light's orbital angular momentum," Science **341**(6145), 537–540 (2013).
14. L. Allen, M. W. Beijersbergen, R. J. C. Spreeuw, and J. P. Woerdman, "Orbital angular-momentum of light and the transformation of Laguerre–Gaussian laser modes," Phys. Rev. A **45**(11), 8185–8189 (1992).
15. H.-L. Zhou, D.-Z. Fu, J.-J. Dong, P. Zhang, D.-X. Chen, X.-L. Cai, F.-L. Li, and X.-L. Zhang, "Orbital angular momentum complex spectrum analyzer for vortex light based on the rotational Doppler effect," Light: Sci. Appl. **6**(4), e16251 (2016).
16. O. Emile and J. Emile, "Fluid vortex mapping using the rotational Doppler effect," Appl. Phys. Lett. **120**(18), 181101 (2022).
17. X. Zhang, J. Jia, K. Zhai, Z. Chang, Z. Guo, and P. Zhang, "Detection and demultiplexing of cylindrical vector beams enabled by rotational Doppler effect," Adv. Photonics Res. **3**(10), 2200049 (2022).
18. Q. Wang, Z. Zhou, D. Liu, H. Ding, M. Gu, and Y. Li, "Acoustic topological beam nonreciprocity via the rotational Doppler effect," Sci. Adv. **8**(40), eabq4451 (2022).
19. D. B. Phillips, M. P. Lee, F. C. Speirits, S. M. Barnett, S. H. Simpson, M. P. J. Lavery, M. J. Padgett, and G. M. Gibson, "Rotational doppler velocimetry to probe the angular velocity of spinning microparticles," Phys. Rev. A **90**(1), 011801 (2014).
20. Z. Guo, J. Meng, M. An, P. Cheng, J. Jia, Z. Chang, X. Wang, and P. Zhang, "Remote angular velocity measurement by the cascaded rotational doppler effect," Appl. Opt. **60**(31), 9892–9895 (2021).
21. Y. Zhai, S. Fu, C. Yin, H. Zhou, and C. Gao, "Detection of angular acceleration based on optical rotational Doppler effect," Opt. Express **27**(11), 15518–15527 (2019).
22. H. Guo, X. Qiu, S. Qiu, L. Hong, F. Lin, Y. Ren, and L. Chen, "Frequency upconversion detection of rotational Doppler effect," Photonics Res. **10**(1), 183–188 (2022).
23. M. P. J. Lavery, S. M. Barnett, F. C. Speirits, and M. J. Padgett, "Observation of the rotational Doppler shift of a white-light, orbital-angular-momentum-carrying beam backscattered from a rotating body," Optica **1**(1), 1–4 (2014).
24. Z. Li, T. Liu, Y. Ren, S. Qiu, C. Wang, and H. Wang, "Direction-sensitive detection of a spinning object using dual-frequency vortex light," Opt. Express **29**(5), 7453–7463 (2021).
25. S. Qiu, T. Liu, Y. Ren, Z. Li, C. Wang, and Q. Shao, "Detection of spinning objects at oblique light incidence using the optical rotational Doppler effect," Opt. Express **27**, 24781 (2020).
26. Y. Ding, Y. Ren, T. Liu, S. Qiu, C. Wang, Z. Li, and Z. Liu, "Analysis of misaligned optical rotational Doppler effect by modal decomposition," Opt. Express **29**(10), 15288–15299 (2021).
27. S. Qiu, Y. Ren, T. Liu, Z. Li, Z. Liu, C. Wang, Y. Ding, and Q. Sha, "Rotational Doppler effect detection by LG beams with a nonzero radial index," Opt. Express **29**(7), 10275–10284 (2021).
28. W. Zhang, J. Gao, D. Zhang, Y. He, T. Xu, R. Fickler, and L. Chen, "Free-space remote sensing of rotation at the photon-counting level," Phys. Rev. Appl. **10**(4), 044014 (2018).
29. O. Emile, J. Emile, and C. Brousseau, "Rotational Doppler shift upon reflection from a right angle prism," Appl. Phys. Lett. **116**(22), 221102 (2020).

Optics EXPRESS

30. X. Qiu, D. Zhang, W. Zhang, and L. Chen, "Structured-pump-enabled quantum pattern recognition," Phys. Rev. Lett. **122**(12), 123901 (2019).
31. L. Torner, J. P. Torres, and S. Carrasco, "Digital spiral imaging," Opt. Express **13**(3), 873–881 (2005).
32. F. Han, W. Wang, T. Liu, Y. Ren, Z. Liu, and S. Qiu, "Symmetry detection of rotating patterns based on rotational Doppler effect of light," Chin. Opt. Lett. **20**(12), 122601 (2022).
33. Z. Yang, O. S. Magana-Loaiza, M. Mirhosseini, Y. Zhou, B. Gao, L. Gao, S. M. H. Rafsanjani, G.-L. Long, and R. W. Boyd, "Digital spiral object identification using random light," Ligh: Sci. Appl. **6**(7), e17013 (2017).
34. F. M. Miatto, A. M. Yao, and S. M. Barnett, "Full characterization of the quantum spiral bandwidth of entangled biphotons," Phys. Rev. A **83**(3), 033816 (2011).
35. V. D. Salakhutdinov, E. R. Eliel, and W. Loffler, "Full-field quantum correlations of spatially entangled photons," Phys. Rev. Lett. **108**(17), 173604 (2012).
36. E. Karimi, D. Giovannini, E. Bolduc, N. Bent, F. M. Miatto, M. J. Padgett, and R. W. Boyd, "Exploring the quantum nature of the radial degree of freedom of a photon via Hong-Ou-Mandel interference," Phys. Rev. A **89**(1), 013829 (2014).
37. J. Jia, K. Zhang, G. Hu, M. Hu, T. Tong, Q. Mu, H. Gao, F. Li, C.-W. Qiu, and P. Zhang, "Arbitrary cylindrical vector beam generation enabled by polarization-selective gouy phase shifter," Photonics Res. **9**(6), 1048–1054 (2021).
38. M. Hiekkamaki, S. Prabhakar, and R. Fickler, "Near-perfect measuring of full-field transverse-spatial modes of light," Opt. Express **27**(22), 31456–31464 (2019).
39. F. Bouchard, N. H. Valencia, F. Brandt, R. Fickler, M. Huber, and M. Malik, "Measuring azimuthal and radial modes of photons," Opt. Express **26**(24), 31925–31941 (2018).
40. S. Choudhary, R. Sampson, Y. Miyamoto, O. S. Magana-Loaiza, S. M. H. Rafsanjani, M. Mirhosseini, and R. W. Boyd, "Measurement of the radial mode spectrum of photons through a phase-retrieval method," Opt. Lett. **43**(24), 6101–6104 (2018).
41. Z. Guo, Z. Chang, J. Meng, M. An, J. Jia, Z. Zhao, X. Wang, and P. Zhang, "Generation of perfect optical vortex by Laguerre–Gauss beams with a high-order radial index," Appl. Opt. **61**(17), 5269–5273 (2022).
42. J. Jia, Q. Li, K. Zhang, D. Chen, C. Wang, H. Gao, F. Li, and P. Zhang, "Integrated design of pi/2 converter and its experimental performance," Appl. Opt. **57**(21), 6076–6082 (2018).
43. D. Zhang, X. Qiu, W. Zhang, and L. Chen, "Violation of a bell inequality in two-dimensional state spaces for radial quantum number," Phys. Rev. A **98**(4), 042134 (2018).
44. Z. Zhang, D. Zhang, X. Qiu, Y. Chen, S. Franke-Arnold, and L. Chen, "Experimental investigation of the uncertainty principle for radial degrees of freedom," Photonics Res. **10**(9), 2223–2228 (2022).
45. M. Krenn, M. Huber, R. Fickler, R. Lapkiewicz, S. Ramelow, and A. Zeilinger, "Generation and confirmation of a (100×100)-dimensional entangled quantum system," Proc. Natl. Acad. Sci. U. S. A. **111**(17), 6243–6247 (2014).
46. S. Qiu, Y. Ding, T. Liu, Z. Liu, and Y. Ren, "Rotational object detection at noncoaxial light incidence based on the rotational Doppler effect," Opt. Express **30**(12), 20441–20450 (2022).
47. M. Krenn, J. Handsteiner, M. Fink, R. Fickler, R. Ursin, M. Malik, and A. Zeilinger, "Twisted light transmission over 143 km," Proc. Natl. Acad. Sci. U. S. A. **113**(48), 13648–13653 (2016).
48. E. Bolduc, N. Bent, E. Santamato, E. Karimi, and R. W. Boyd, "Exact solution to simultaneous intensity and phase encryption with a single phase-only hologram," Opt. Lett. **38**(18), 3546–3549 (2013).
49. H. Qassim, F. M. Miatto, J. P. Torres, M. J. Padgett, E. Karimi, and R. W. Boyd, "Limitations to the determination of a Laguerre–Gauss spectrum via projective, phase-flattening measurement," J. Opt. Soc. Am. B **31**(6), A20–A23 (2014).
50. L.-M. Zhou, Y. Shi, X. Zhu, G. Hu, G. Cao, J. Hu, and C.-W. Qiu, "Recent progress on optical micro/nanomanipulations: structured forces, structured particles, and synergetic applications," ACS Nano **16**(9), 13264–13278 (2022).